Hydrogen embrittlement revealed via novel in situ fracture experiments using notched micro-cantilever specimens

Y. Deng, A. Barnoush

Abstract:

The susceptibility of the FeAl intermetallic alloy to hydrogen-assisted cracking was investigated by in situ fracture experiments using notched micrometre-sized specimens using an Environmental Scanning Electron Microscope (ESEM). The notched beams were loaded under two different environmental conditions: one in high vacuum (5×10^{-4} Pa) to avoid hydrogen effects and one under a certain water vapor pressure (450 Pa) to promote hydrogen uptake. The fracture behaviour on a non-ASTM-standard micro-sized specimen was successfully studied by the experimental approach, and the microstructure of the whole crack area was analysed by Transmission Kikuchi Diffraction (TKD) and Transmission electron microscopy (TEM) techniques. Three crack growth stages were observed in all the specimens: i) elastic regime, ii) notch blunting and micro-crack formation; and iii) stable crack growth. We observed an accelerated crack propagation rate in specimens under hydrogen exposure. The hydrogen embrittlement phenomenon was found to occur because of the strong hydrogen-dislocation interactions. The combined effect of hydrogen-enhanced dislocation nucleation and hydrogen-restricted dislocation mobility is responsible for the hydrogen-enhanced cracking behaviour.

Keywords: hydrogen embrittlement, micro-fracture mechanics, Transmission Kikuchi Diffraction or Transmission EBSD, FeAl intermetallics.

Graphic abstract:
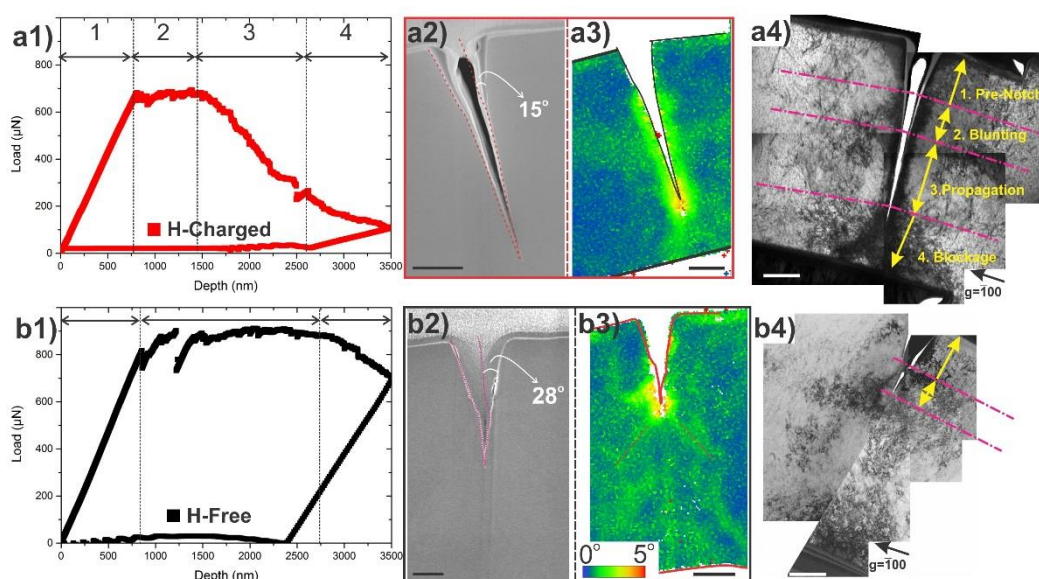
Fig. 0. The crack propagation stages shown in the load-displacement curves for H-charged a1) and H-free a2) cases; the corresponding crack morphology a2) b2), deformation substructure revealed via t-ESBD a3) b3) and TEM bright field a4) b4) techniques for H-charged and H-free cases, respectively. All the scale bars are 500 nm.

1. Introduction:

Mechanical properties of metals and alloys are on some level determined by interstitial atoms. Hydrogen (H), as one common interstitial element, is often found to degrade the fracture behaviour and lead to premature or catastrophic failure in a wide range of materials. Hydrogen embrittlement (HE) has thus been an important issue in hydrogen technology and has evoked intense scientific studies. However, with all the research efforts, HE is still one of the controversial questions and is particularly severe in iron-based alloys and steels because of the low solubility and high diffusibility of H in Fe [1]. For the metallic materials that do not form hydrides, the HE effects are always described commonly in one or a combination of the following models: 1) Hydrogen-enhanced decohesion (HEDE); 2) Adsorption-induced dislocation emission (AIDE); 3) Hydrogen-enhanced localized plasticity (HELP); and 4) Defactant mechanism.

The HEDE mechanism postulates that the hydrogen atoms attached to the crack tip reduce the cohesive bond energy between atoms and encourage a cleavage-like failure [2-7]. However, this mechanism can occur only when the stress intensity for the fracture ahead of the crack tip falls below the value to stimulate dislocation activities, which is not realistic in bcc alloys at room temperature since the dislocation emission seems still easier even at full saturation of H [8]. However, the HEDE finds its huge popularity in explaining the intergranular fracture [9-12], which is rational since the strain constraint near the grain boundaries or phase boundaries requires multiple slip system activation, which produces opportunities for the cracking to occur through bond breaking. The AIDE states that hydrogen reduces the dislocation formation energy at the crack tip, thus promoting the crack propagation with dislocation emission from the crack tip at relatively lower stresses [13, 14]. The above two models are obtained mainly from the posterior interpretation of the post-mortem morphological features obtained from macroscopic tests and lack some supporting evidence from direct experimental observations, or are supported mostly by simulations and models with several simplifications that remain to be validated. As an exception, the HELP is basically built on in situ observations of the dislocation motion in environmental transmission electron microscopy (ETEM) cells and states that the hydrogen atmosphere attached to the dislocation effectively shields the stress field in certain directions and thus allows the stress field to move in such directions at a lower stress level [15-22]. As a descriptive mechanism, the HELP has found widespread support since its first announcement. However, there are still disagreeing voices. The accelerated dislocation mobility in HELP via H reduced the degree of interaction of dislocations with other elastic singularities due to the H shielding effect [23], which is found not to be realistic in bcc metals since a large amount of H concertation (1.5×10^{-2} H/Me to reach the softening effect of 70 MPa) is required [24]. The experimental observation of

"softening and hardening" as a common HE phenomenon in bcc iron was explained based on atomistic simulation with H-enhanced double-kink formation at high T or low H content, and H reduced kink-pair mobility at low T or high H content [25, 26]. Song and Curtin [27, 28] proposed that hydrogen reduces rather than enhances dislocation mobility based on atomic calculations. Recently, an opposite observation from an ETEM cell that dislocation will be locked by introducing H, and they argue that the locking effect is introduced by hydrogenated vacancy rather than atomic H [29], bringing about another hot but yet debated mechanism about hydrogen and strain-assisted vacancy production [30]. The defactant theory relies on statistical thermodynamics that predicts a reduction of defect formation energy to improve the generation rate, which has been observed directly from in situ TEM [31], and indirectly confirmed by in situ nanoindentation tests [32]. These mechanisms are hydrogen concentration, loading condition, and material dependence and are not necessarily mutually exclusive.

One of the major causes of the endless arguments of HE mechanisms roots in the difficulty of capturing the effect in the different time- and length-scales associated with the phenomenon. Hydrogen diffusion is considered fast and can vary from the test temperature and stress/strain state. The nontrivial H atoms-metal atoms, H atoms-defects and/or H atoms-crack interactions require an analysis under relevant atomic and/or the mesoscopic length scale either by computational modelling or by advanced experimental characterization. The existing experimental methods are either macroscopic tests providing only some phenomenal observations with low resolution, which lack revealing mechanistic understanding, or nanoscale tests inside ETEM offering chances to see direct H-defect interactions, which cannot ensure a certain constant strain/stress state or avoid the proximity effect from the sample surface with the tiny sample size used. Recent studies [33, 34] of the micro-cantilever bending test with in situ hydrogen charging provide a good compromise by using the micro-sized sample that is small enough to sensitively capture the H effects while at the same time having enough volume capacity to avoid the shortages from ETEM tests. Another advantage of using a micro-sized sample is the possibility of the postmortem analyses of the overall sample rather than a selected part.

In this paper, the same experimental setup was employed with notched micro-sized cantilevers, and a simple case of H-induced cracking was investigated in detail, and a mechanism for crack initiation and propagation is proposed. The pure FeAl intermetallic single crystalline material was chosen as a model material to achieve a clean H-charging condition by the chemical reaction of Al with the water molecules (H_2O), provided by environmental scanning electron microscope (ESEM) as a default atmosphere, as well as to avoid the uncertainties caused by microstructural complications. More details can be viewed in previous papers [33, 35].

2. Experimental details
2.1. Specimen preparation and testing techniques

The single crystalline FeAl was grown by a modified Bridgeman technique followed by an annealing process at 673 K for 120 h to eliminate the thermal vacancies [36]. From this specimen, cantilevers were milled by a focussed ion beam (Helios Nanolab Dual Beam FIB, FEI Inc., USA) to dimensions of ~3X3X12 µm using 93 pA at 30 kV as the final current to maintain a good surface quality. A lower current of 28 pA was used to introduce a sharp notch to each cantilever, 1.0 µm away from the cantilever beam support. The pre-notch was aligned to analyse the (001) [100] crack system, and the depth of the pre-notch was measured prior to testing from the side view. The notation of the crack system, (hkl) [uvw], gives the crystallographic plane (hkl) wherein the crack is located and the crack front direction [uvw]. The final geometry and test condition of all the beams are presented in Table 2.1.
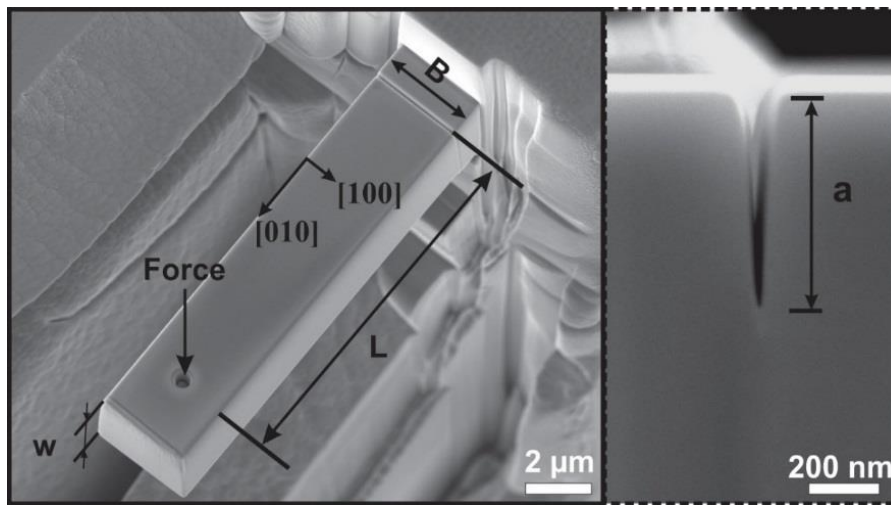

Fig. 1. Secondary electron image of a FeAl cantilever with characteristic dimensions

After ex situ electron backscattered diffraction (EBSD) characterization, the beams were loaded in situ using the PI-85 Pico-indent system (Hysitron Inc., USA) inside the ESEM (Quanta FEG 650 ESEM, FEI Inc., USA) under two different loading conditions: static loading and low cyclic loading. The static loading was applied with a 1.0 nm/s loading rate in the displacement-controlled mode. The dwell time between the loading and final unloading steps was 10 s. The low cyclic loading was applied by implementing partial unloading sequences after yielding with equal displacement interval of 400 nm. The loading and partial unloading speed were settled to be the same. Bending tests were performed under vacuum (~5X10^{-4} Pa), i.e., hydrogen free, and water vapor ESEM (450 Pa, 900 Pa) conditions, i.e., hydrogen charged.

Tab. 2.1. Beam dimensions (in µm), test conditions and test methods. The symbols L, B, w, a, represent the length, width, thickness, and initial notch depth of the beam shown in Fig. 1.

Beam No.	L	B	w	a	Test Conditions	Final Depth	Test Methods
V1	11.34	2.97	3.212	689.0	Vacuum	3.5	Static loading
V2	11.31	2.84	3.193	593.6			
E1	11.50	2.91	3.135	632.7	ESEM (450 Pa)		

E2	11.41	3.06	3.168	649.4		
E3	11.47	2.88	3.135	580.6	ESEM (900 Pa)	2.0
V3	11.02	3.25	3.00	383.1	Vacuum	
V4	11.03	3.209	3.01	410		4.5	Cyclic loading
E3	11.05	3.031	3.016	395.0	ESEM (450 Pa)	
E4	11.05	3.157	3.094	392.9		

2.2.   t-EBSD and TEM characterization

To visualize plastic deformation with relatively high resolution, a novel transmission EBSD (t-EBSD) was performed on the cracking area after tests. The major difference between t-EBSD and normal EBSD is that the sample used is electron-transparent and mounted horizontally or back-tilted away from the EBSD detector. With this geometry, the diffraction patterns are generated mainly from the bottom surface of the sample with a small source volume, which improves the spatial resolution from ~20 nm in normal EBSD down to ~2 nm in t-EBSD. As first introduced by Keller and Geiss [37], t-EBSD has received significant interest and application in a wide range of fields, especially in nanocrystalline and ultrafine grain materialsAnother potential application of t-EBSD lies in the analysis of the deformation substructure in highly deformed materials. Normal EBSD analysis on those highly deformed areas is always problematic due to the high dislocation density and lattice distortion, which results in a blurring and even missing of the Kikuchi patterns and leads to a poor indexing accuracy. The situation becomes less troublesome when t-EBSD is applied due to the smaller interaction volume, which enables the indexing of areas with severe plastic deformation.

Two of the cantilevers bent in different environmental conditions (vacuum and 450 Pa ESEM) were gently transferred to a three-post copper grid using a lift-out finger (AutoProbe 200), and then samples were milled from both sides to the final thickness of approximately 100 nm using FIB. The same samples were analysed with both t-EBSD and TEM methods. t-EBSD was performed on an FEI Quanta FEG 650 ESEM with a voltage of 30 kV and current of 6.4 nA. The sample was tilted to 25° to the electron beam direction. The transmission Kikuchi patterns were captured using an NORDIF EBSD detector with a 20-nm step size. The Kikuchi band data obtained was indexed by TSL OIM data Collection 7.1.0 and was analysed with TSL OIM Analysis 7.1.0 software. Further dislocation analysis was performed with the TEM technique (JEM-2100, JEOL, Inc.)

3. Results:
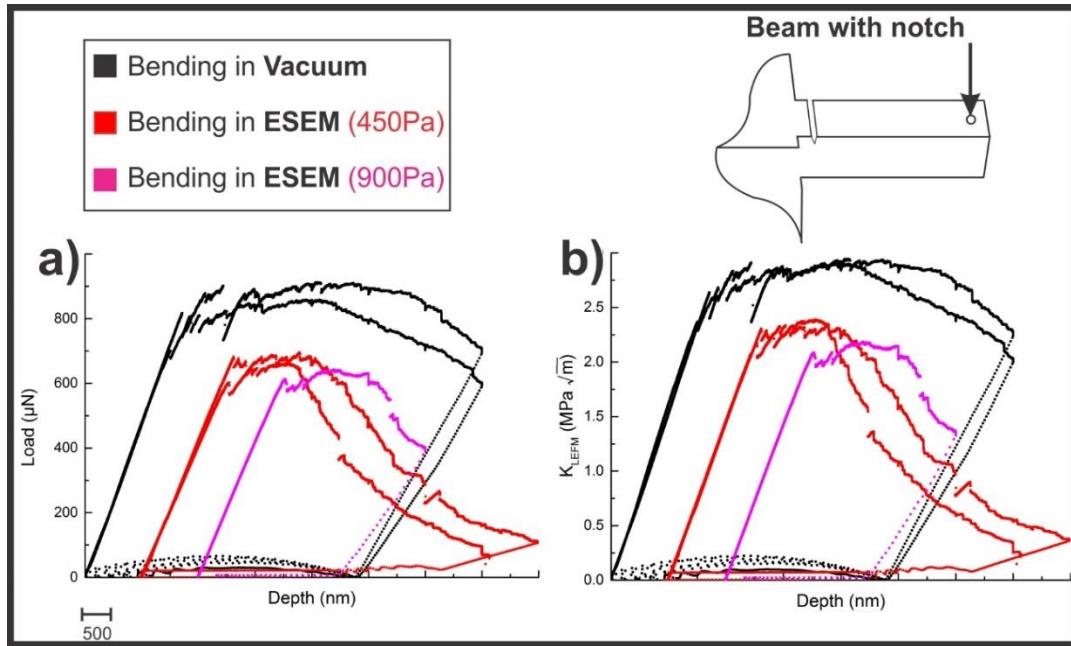### 3.1.   In situ testing and fracture analysis of the notched cantilevers

Fig. 2. The experimental Load-Displacement curves for beams bent in a vacuum and ESEM (450 Pa, 900 Pa), respectively a), the converted fracture toughness based on linear elastic fracture mechanics with respect to displacement b).

Fig. 2(a) shows three different sets of experiments in which cantilevers were tested under three environmental conditions, i.e., in vacuum, or in ESEM with 450 Pa and 900 Pa water vapor pressures. For a better comparison, the flow curves tested in two ESEM modes are shifted by 500 nm on the depth axis, respectively. A good agreement of the elastic stiffness is found in all beams, which indicates a precise and similar geometry of all the beams tested in our experiment. The beams tested in the vacuum show a ductile behaviour with a little strain hardening effect after yielding. A force plateau is followed after reaching the maximum force (F_{max}), which is also characterized by the onset of crack growth. Then, the force drops continuously due to the propagation of the crack.

The mechanical response of beams bent in ESEM follows the similar behaviour but with lower F_{max}, a shorter force plateau region, and an accelerated crack-propagating rate. The detailed crack propagation processes under the two conditions will be discussed in detail in Section 3.4. Nevertheless, a very similar behaviour is found between the beams bent in the 450 Pa and the 900 Pa water pressure condition, implying that a balance has been reached between two rates: the rate of producing fresh metal surface under a certain loading strategy (1 nm/s) and the rate of H generation by chemical reaction of H_2O molecules with fresh metal, and no more H will be generated by only increasing the water vapor pressure. Therefore, the following cyclic loading tests were only performed under two conditions: vacuum and 450 Pa ESEM. In the further text, they are designated as H-free and H-charged conditions, respectively.

To quantitatively estimate the stress intensity factor near the crack tip, the linear elastic fracture mechanics (LEFM) approach was first applied. The fracture toughness K_{IC} according to the LEFM is calculated using the following equation [38]:

$$K_{IQ} = \frac{F_Q L}{B w^{3/2}} f(a / w) \tag{1}$$

where F_Q is the conditional force, which is the load from where the line has 95% of the initial loading slope according to the ASTM standards. L characterizes the loading span between the notch and the loading point, a is the notch length, and w represents the thickness and width of the cantilever, as shown in Fig. 1. $f(\frac{a}{w})$ is a dimensionless geometric factor, which was determined for a rectangular beam geometry with a straight notch by means of finite element modelling [39]:

$$f(a \, / \, w) = 77.608(a \, / \, w)^3 - 48.422(a/w)^2 + 24.184(a/w) + 1.52 \qquad (2)$$

By using Eq. (1), the load showing in Fig. 1a is normalized with respect to the sample geometry. A plot of the stress intensity factor (K_{LEFM}) as a function of the indenter displacement for beams bent under different environmental conditions is shown in Fig. 1(b). The conditional fracture toughness K_Q, which was obtained following ASTM standards, reaches 2.41 MPa√m for the vacuum condition and 1.99 MPa√m for the ESEM 450 Pa condition.
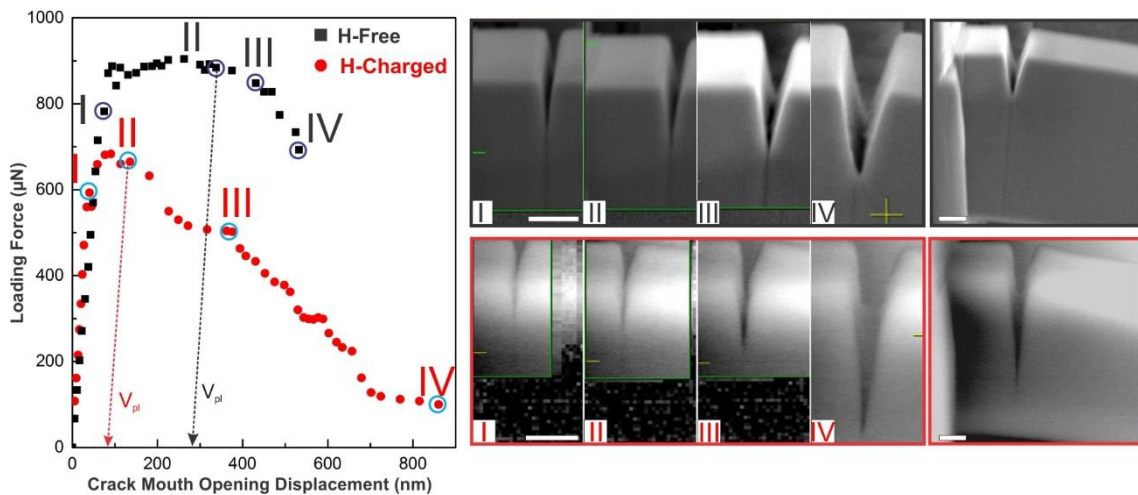
3.2.   *In situ CMOD measurement*
3.3.

Fig. 3. Force versus CMOD for two cantilevers bent in H-free and H-charged conditions. The secondary electron (SE) micrographs showing the characteristic crack propagation stages indicated in the L-CMOD curves were taken from the videos recorded for these tests. All scale bars are 500 nm.

The Crack Mouth Opening Displacement (CMOD) was determined by in situ SEM analysis for both H-free and H-charged conditions. Fig. 3 shows the Force-CMOD relationship with the corresponding SE micrographs at each marked stage. For the H-free case, a little crack opening was observed after yielding (stage I) before reaching the end of the force plateau (stage II), which is suggested as due to notch blunting. Then, a more pronounced CMOD and hence a large crack growth is found in company with a little drop in force (stage III), and then the crack

continues growing with a decreasing force (stage IV). The force plateau is reached in the H-free case due to two oppositional effects. A pronounced plasticity caused strain-hardening as well as blunting of the newly created crack tip, which leads to an increasing force for further deformation, while the crack propagation brings a reduction in beam cross-section, which results in a decrease in force. For the H-charged case, no obvious force plateau was observed, and a little CMOD was recorded before reaching the maximum force (stage II), and a pronounced crack propagation occurred after passing the maximum force with a continuous decreasing force. The conditional CMOD can be calculated by use of the equation:

$$\delta_Q = \delta_Q^{el} + \delta_Q^{pl} = d_n \frac{K_{IQ}^2(1 - v^2)}{\sigma_Y E} + \frac{r_{pl}(w - a_0)v_{pl}}{r_{pl}(w - a_0) + a_0} \tag{3}$$

where d_n is a dimensionless factor, which depends on the strain-hardening rate and the ratio of σ_Y / E and was set to 0.5 when assuming the plane strain condition. r_{pl} is the rotation factor according to the hinge model and was set to 0.44 for our geometry assembly to the SE(B) geometry. The plastic part of displacement on the force-CMOD curve, v_{pl}, is characterized by constructing a line parallel to the loading line. The calculated conditional CMODs are 280 nm and 85 nm for H-free and H-charged conditions, respectively.

$$K_{Q,\delta} = \sqrt{1 / d_n \sigma_Y \frac{E}{(1 - v^2)} \delta_Q} \tag{4}$$

The fracture toughness $K_{IQ,\delta}$ for the two samples was calculated to be 13.92 MPa√m and 8.64 MPa√m for the H-free and H-charged case, respectively.

3.4.   Fracture surface of the beams
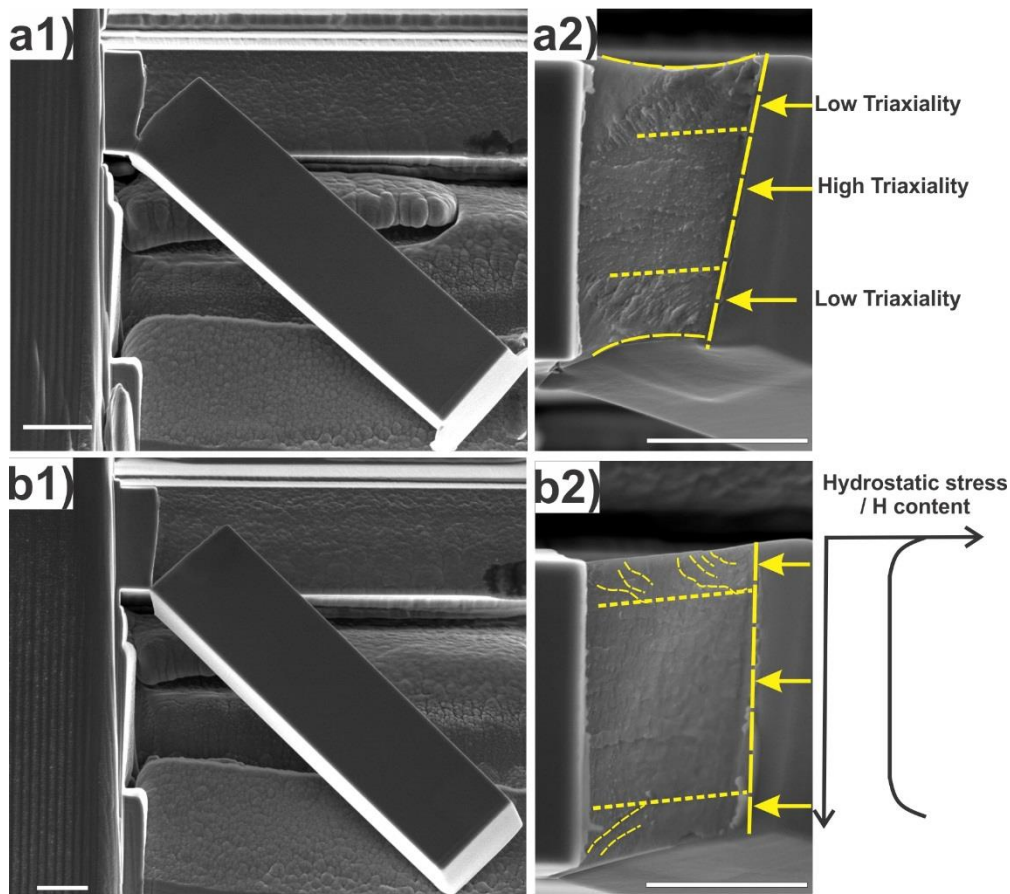
Fig. 4. The side view of beams and fracture surface bent in vacuum a) and in ESEM mode b). For the H-free case, two static loading procedures plus one quick hit must be applied to open the crack mouth large enough to observe the fracture surface. All scale bars are 2 µm.

Fig. 4 a1) and b1) shows the side view of the cantilevers after deformation. A very straight top surface observed indicates that all the deformation is localized to the crack propagation zone. A fracture surface is presented in Fig. 4 for two micro-beams bent in vacuum and ESEM 450 Pa modes. For the beam bent in vacuum, two static bending procedures (see Supplementary Materials) plus one quick hit were applied to open the crack mouth farther, which left a featureless flat plane located on the lower parts of the fracture surface. The rest fracture morphology due to the bending is characterized in two regions: one consists of relatively flat areas and protruding elevations lying along the cracking direction in the central region, and the other two are slant fractured regions on the edges, divided by yellow dashed lines in Fig. 4. The observed crack morphology is quite similar to a dimple fracture formed with micro-holes coarsening ahead of the crack tip, in which case an isolated crack front will form ahead of the main crack front. This was not the case in our observation. Therefore, these pyramid-like enclaves are supposed to be left behind by the crack tip and are necking down in an ideal ductile manner after the crack front has already passed.

The two slant areas are formed due to the low triaxiality stress state near the edges. The high stress triaxiality on the central part of the beam facilitates the crack growth within the plane strain condition with higher constraint, while the lower triaxiality on the edges of the beam

resembles the plane stress condition with lower constraint. A typical crack "tunneling" effect, where the crack grows faster at the centre of the beam due to the higher stress triaxiality, is observed in the H-free sample (see Fig. 4a).

Assuming the central part of the beam is under a pure plane strain condition while the edge surface is under a pure plane stress condition, applying the von Mises yielding criterion:

$$\sigma_{yy} \ (at \ yield) = \begin{cases} \sigma_{YS} & (plane \ stress \ condition) \\ 2.5\sigma_{YS} & (plane \ strain \ condition) \end{cases}$$

the edge surface will experience lower crack-tip stress with more crack-tip yielding than the central region. With a further increase in the displacement, the σ_{yy} in the central region will continue increasing until 2.5 σ_{yy} is reached. Meanwhile, the plastic zone on the edge surface starts to expand. The result for this case is a larger plastic zone after deformation on the edge surface than in the central region. As the K_I reaches the critical value in the central region, a tiny crack starts to nucleate and to propagate along the notch plane in the central region due to the high global constraints, with a 45° angle towards the free surface controlled by the maximum principal stress direction.

$$t_{plastic \ zone} = \begin{cases} \dfrac{K_{IC}^2}{\pi\sigma_Y^2} & (plane \ stress \ condition) \\ \dfrac{K_{IC}^2}{3\pi\sigma_Y^2} & (plane \ strain \ condition) \end{cases}$$

The beam deformed in the ESEM mode, however, shows a totally different type of fracture surface morphology with a quite flat surface throughout the whole beam, indicating crack growing in a more brittle manner. We also observed some crack propagation trails inclined from beam interior to the edge surface, however, with a more limited region compared to the H-free case, which indicates a similar cracking behaviour as described above with less difference in the plastic zone size between the beam centre and beam edges. This diffeence, in our view, is caused by the different hydrostatic stress states and the corresponding difference in H content [40]. During the bending test, as long as the thin oxide layer is destroyed and H is produced, the high degree of hydrostatic stress state near the beam edges will increase the H uptake locally, while the centre part of the beam with lower hydrostatic stress will attract fewer H atoms. A reduction in the plastic zone size will appear in both areas due to the presence of H but with different reduction degrees according to the H concentrations. A higher H concentration causes higher shrinkage of the plastic zone size and vice versa. In this manner, a remission in the plastic zone size difference is observed, which in return is shown on the fracture surface, as the difference between the centre and edges is softened with the presence of H, as seen in Fig. 3b2.

3.5.   J-integral

When the plastic zone size is large with respect to the sample dimensions, LEFM is no longer applicable, and the Elastic-Plastic Fracture Mechanics (EPFM) has to be applied to evaluate the fracture toughness. To evaluate the fracture toughness by the J-integral, a precise knowledge of crack propagation is required. This requirement can be realized by performing several unloading segments to obtain the corresponding compliances. In general, a growing crack leads to an increasing a/W ratio and a decreasing bending stiffness. To understand the correlation between the compliance and the a/W ratio, anisotropic linear elastic FEM simulation was performed with elastic stiffness inputs: C_{11}=171 GPa, C_{12}=117 GPa and C_{44}=121 GPa [41].
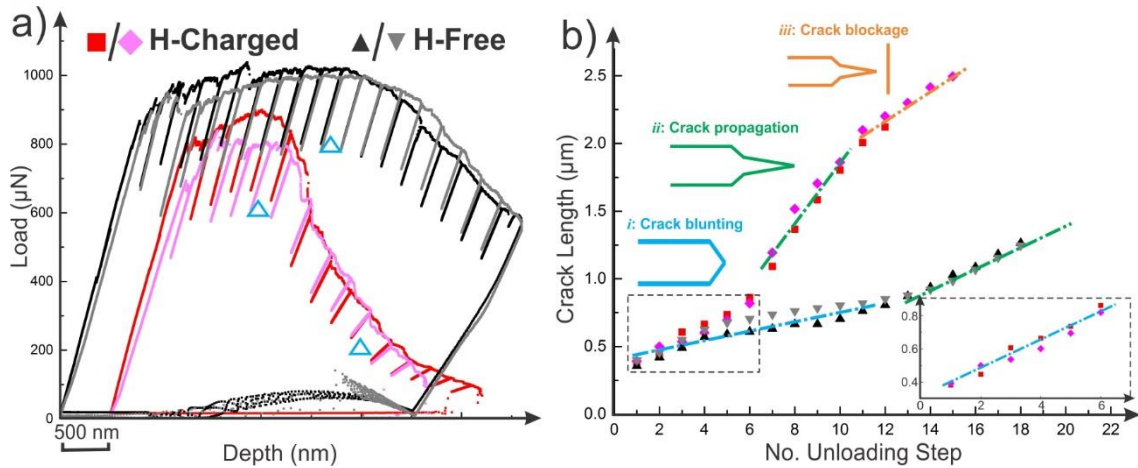

Fig. 5. Load-displacement curve of the low cyclic loading for beams with H-Charged and H-Free conditions a); the corresponding crack length determined by use of the compliance method, FEM simulation b). Three different crack propagation stages with different propagation rates were found for the H-charged condition, and two stages for the H-free condition; the location corresponding to the change between each stage is marked with triangles in a).

The load-depth curves from the low-frequency cyclic loading tests are shown in Fig. 5a, which demonstrates the behaviour similar to the static loading tests. The crack length of each unloading segment was calculated by the FE simulations, and the results are depicted in Fig. 5b. Three distinct regions can be recognized, possessing different crack propagation rates for the H-charged case, while for the H-free case, two regions can be found. The *i* part marked with the blue line shows a slower crack propagation rate (~80 nm/step for H-charged specimens and 39 nm/step for H-free specimens), while a remarkable increase in cracking rate is observed in the *ii* part (~225 nm/step and ~75 nm/step). The change occurred around the 6th unloading step for H-charged samples, while for H-free samples, the change delays to the 11th unloading step, which marks the end of the force plateau and the start of decreasing force for both cases while referring to the load-depth curves (see the Δ markers in Fig. 5a). The force plateau is maintained because of competition of two opposite effects: the local strain hardening caused by plasticity brings about increasing force with further bending, while the reduced ligament by crack propagation reduces the total force. Despite a higher crack growth rate in the *i* stage, the H-charged sample can still maintain a similar (or even higher) total hardening, as seen in the curves in Fig. 5a, which indicates the strain hardening near the crack tip in the H-charged sample is larger than in the H-free case. The higher strain hardening effect for the H-charged sample can be caused by either higher dislocation density by the H-enhanced dislocation nucleation/multiplication, or the H-induced dislocation pinning effect, or a combination of both effects. In addition to the common two stages revealed in both cases, *iii* stage is observed only in H-charged samples with a slightly reduced crack growth rate (~105

nm/step) after the crack length reaches approximately 2 μm. The change occurred at approximately the 11th unloading step, which also shows a decrease in the force-descending rate. This occurred when the crack approached the free bottom surface, which shed a retarding force on the crack tip and tried to block further crack propagation.
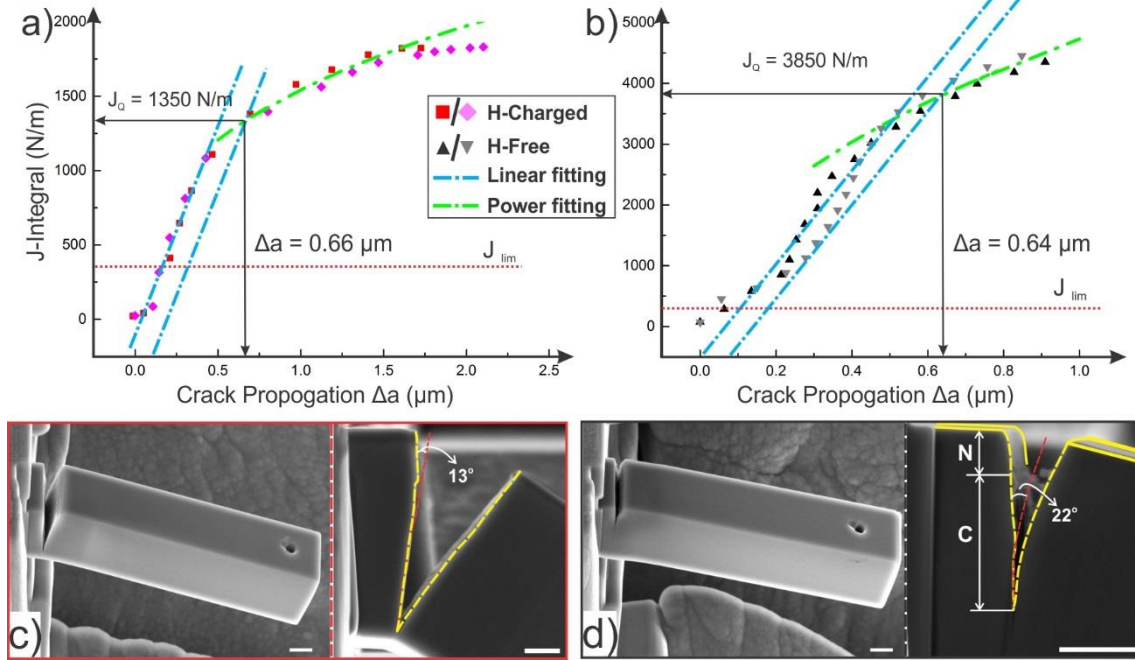

Fig. 6. Crack resistance curves J-Δa for H-Charged a) and H-Free b) conditions shown in Fig. 4; the final fractured beams of the two cases with magnified cracking regions to determine the blunting via the crack tip opening displacement c) and d). All scale bars are 500 nm.

To obtain the crack resistance curve, the J-integral was calculated for each case according to the following equation:

$$J_i = J_i^{el} + J_i^{pl} = \frac{K_i^2(1-v^2)}{E} + \left[J_{i-1}^{pl} + \frac{\eta(A_i^{pl} - A_{i-1}^{pl})}{B(w - a_{i-1})} \right] \left[1 - \frac{a_i - a_{i-1}}{w - a_{i-1}} \right] \quad (5)$$

$$K_{Q,J} = \sqrt{J_Q \frac{E}{1 - v^2}} \quad (6)$$

where K_i^2 is determined by Eq. (1) and (2), η is a constant factor equal to 2 and v is the Poisson ratio set to 0.3. A_i^{pl} defines the area beneath the force-displacement curve excluding the elastic part. The results are shown in Fig. 6. In standard tests, the notch blunting effect is associated with a construction line showing the initial slope of the J-Δa curve. Then, a parallel shift of the construction line by 0.2 mm can be drawn as an offset line. The parallel shift distance Δ is associated with crack opening displacement δ due to a blunting effect with Δ~δ/2. With the crack opening angle measured directly from the crack front (10° for the H-charged case and 22° for the H-free case), the crack opening displacements δ are 0.07 μm and 0.16 μm for each case. Consequently, the offset lines are drawn by shifting the construction lines by 35 nm and 80 nm for each case.

Excluding the initial notch blunting part, the rest of the J- Δa curve should be fitted using the power law of the form:

$$J(\Delta a) = C_1 \left(\frac{\Delta a}{k}\right)^{C_2} \tag{7}$$

where k is a constant equal to 1.0 mm, and C1 and C2 are determined by a regression procedure. In our calculation, k was set to 1.0 μm, and the corresponding fitting parameters are C1=1543.05, C2=0.355, and C1=4717.63, C2=0.483 for each case. These fitting values meet the requirement of C2< 1.0 from E1820 [42]. As discussed previously, the latter few points for the H-charged cases are due to the crack blockage from the bottom surface; those points were not considered into the regression procedure.

The intersection of the regression line and the blunting offset line results in crack resistance J_Q of 1350 N/m for the H-charged case and 3850 N/m for the H-free case and the corresponding crack propagation Δa is 0.66 μm and 0.64 μm for each case. With equation (6), the fracture toughness is calculated as: $K_{Q,J}$ = 15.5 MPa√m and $K_{Q,J}$=26.3 MPa√m for each case.

4. Discussion:

4.1. Evaluation of fracture toughness

The fracture toughness results from the different fracture mechanics approach of this work, together with data from LEFM of the macroscopic sample and atomic simulation with the {100} <001>-crack system, are summarized in Table 4.1. As expected, LEFM does not provide a correct fracture toughness values rather a lower bound for the critical stress intensities. The underestimation from LEFM can be attributed to the small sample size that fails to fulfil the requirement from the testing standards defining the small-scale yielding prerequisite. However, these values, marked as the first deviations from the ideal elastic behaviour, can deliver good approximations of the stress intensities for deformation activity and dislocation motion.

A very good agreement is observed between the fracture toughness from the ASTM standard sample and the one obtained from the J-integral analysis for the H-charged case, while for the vacuum case, a certain underestimation is found. This discrepancy may result from small sample size or the pre-existence of H within the cantilever.

Table 4.1. Experimentally determined fracture toughness from micro-cantilever specimens based on three analysis methods (LEFM, CTOM, and J-integral) and from ASTM standard specimens. The same FeAl single crystalline alloy with {100} <001>-crack system was analysed both in microscopic and macroscopic specimens.

Test Conditions	$K_{Q, LEFM}$	$K_{Q, CTOD}$	$K_{Q, J\text{-integral}}$	ASTM E-399	Ab initio [43]
H-Free	2.41	13.92	23.6	>40*	1.4
H-Charged	1.99	8.64	15.5	16.6	

For a valid evaluation of the fracture toughness calculation based on Eq. (6), the sample dimensions should be larger than a defined characteristic size (t), as illustrated in the following:

$$B, W - a > t = 10 \frac{J_Q}{\sigma_Y}$$

To estimate, the precise yield strength of the material is needed. Considering a macroscopic yield stress of 400 MPa for the FeAl (100) single-crystal [44], the characteristic size is in the range of 96.25 µm for the H-free case and 33.75 µm for the H-charged condition, which lie more than one order of magnitude higher than the sample size used in this work. This mismatch will arise from the typical size effect, namely, the material strength rises with a decreasing sample size, which has been observed in many material systems and was also shown for micro-cantilevers as yield strength increasing with decreasing sample size [45]. Moreover, Iqbal et al. argued that the size effect caused by the strain gradients around the pre-notch with a small radius would also contribute to the mismatch [39] and proposed extracting the microscale yield strength from nanoindentation experiments, where the size effect shows as the hardness increases with decreasing indentation depth. Here, we proposed a new method of using the L-D data from the bending tests of an un-notched beam of the same geometry and with the same loading rate (see Strain-Stress curve for un-notched beam in the Supplementary Materials). The bending strength at the yielding point was measured to be 1600 MPa.

Table 4.2. Minimum critical thickness for prediction of plane-stress, plane-strain state

Environmental Conditions	E (GPa)	σ_Y (MPa) Macroscopic [44]	t2	σ_Y (MPa) Microscopic	t2
H-Free	163	400	96.25	1600	24.06
H-Charged	163	400	33.75	1600	8.44

By considering the yielding strength measured from the micro-cantilever bending test, the characteristic size for the H-charged case is comparable to the size dimension, while it falls roughly one magnitude larger for the H-free case. The constructed specimen size may explain the underestimation of the fracture toughness for H-free case. Another possible reason for the reduced fracture toughness measured in the H-free case is the pre-existing H within the beam matrix. As long as the beams are taken out from the FIB chamber, the chemical interaction with moisture in the air can produce H in the material. This process will continue until a thin alumina layer covers the whole beam surface. The same chemical reaction will also occur for the macroscopic ASTM specimen. However, the much smaller surface-to-bulk ratio in the macroscopic specimen will introduce much less H/metal concentration, and thus the HE effect due to the pre-existing H content is so faint that it can be considered negligible. For the microscopic specimen, the higher surface-to-bulk ratio results in a higher H/metal concentration, which gives rise to the HE effect and lower fracture toughness measured in the micro-size specimen.

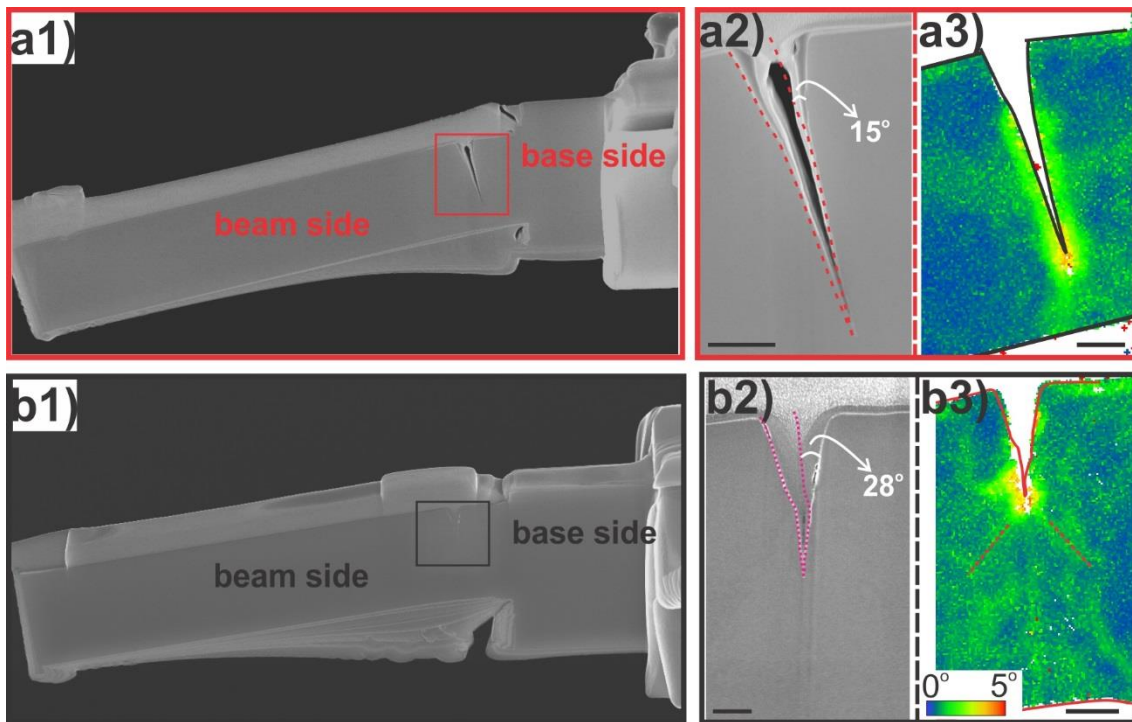## 4.2. Cracking behaviour based on microstructure evolution

Fig. 7. SE images from the cross-section of the lift-out beams tested in two cases: H-charged a1) and H-free b1) cases with enlarged crack morphology images a2) and b2); t-EBSD characterization of the cracking regions are shown in Kernel Average Misorientation (KAM) maps a3) and b3). All the scale bars are 500 nm.

To further understand the cracking behaviour, the deformed beams were lifted out and mounted individually on a three-port grid. The side of the beam was further milled with FIB to reach roughly the centre part of the beam, as shown in Fig. 7 a1) and a2). High-resolution images were taken close to the cracking area (see Fig. 7 a2) and b2)), showing clearly the different crack propagation paths under two sets of environmental conditions. Cracking behaviour with the H-charging condition shows a long crack with a sharp tip, and the initial crack blunting leaves a crack mouth opening angle of approximately 15°. For the H-free condition, a much shorter crack was observed with a crack mouth opening angle of 28° resulting from the initial crack blunting. The values are quite consistent with the previous measurements from the side of the beams (see Fig. 6). To visualize plastic deformation with relatively high resolution, t-EBSD is one of the novel tools allowing the correlation of local lattice rotations to the deformation in crystalline materials. Fig. 7 a3) and b3) shows the t-EBSD results from the same cracking areas. For the H-charged case, a very confined plastic zone is observed along the crack propagation with high localized geometrically necessary dislocation (GND) density found in front of the crack tip. For the H-free case, in addition to the similar highly GND zone around the crack tip, the plasticity can be resolved far ahead of the crack tip. Two slip systems (marked with red dot lines) are found to have approximately a 90° angle with each other, indicating the slip planes are (110), (11-2) or (112) near the beam side and (1-10), (1-1-2) or (1-12) near the base side. As predicted from slip line theory, the crack opening angle during ideal ductile crack growth should be equal to or larger than the angle

between two activated slip planes [46]. The observed smaller crack opening angle here indicates that other fracture mechanisms, such as microvoid formation or micro-cleavage, accompany the crack propagation.
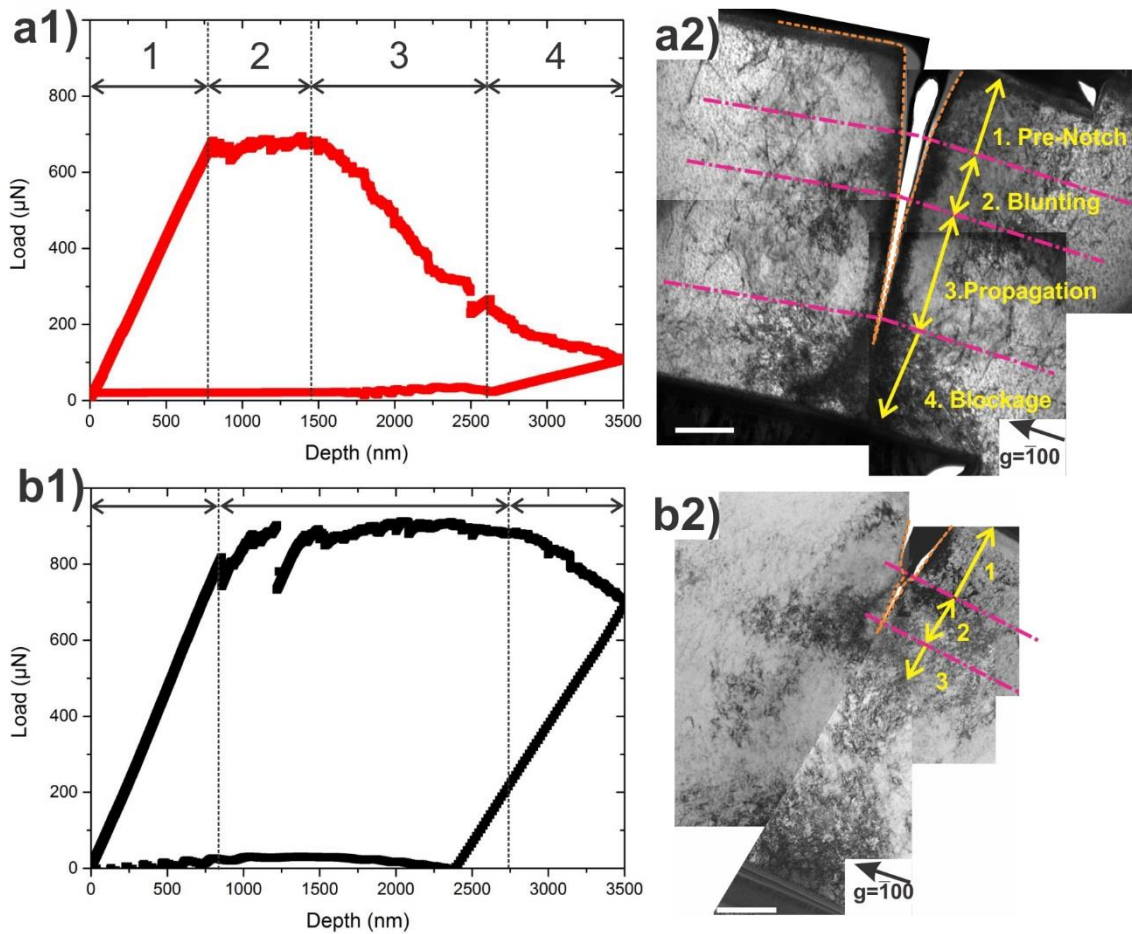
Fig. 8. The crack propagation stages showing on the L-D curves for H-charged a1) and H-free b1) cases, together with the final crack passageway with the dislocation substructure within the corresponding crack propagation stages shown with TEM bright field (BF) (g= <-110>) images a2) and b2). All the scale bars represent 500 nm.

As discussed in Section 3.4, the load-displacement exhibits four distinct regimes with different crack-propagating processes for the H-charged case, while for the H-free case only three are present. The 1st regime corresponds to the elastic loading with no plastic deformation or cracking behaviour taking place. The 2nd part includes a force plateau and ends with the point of force descending. The force plateau is reached because of two competing effects: the plastic deformation ahead of the notch tip and a reduced ligament due to the notch extending and micro-crack initiation and propagation. The crack passageway segments corresponding to this stage are shown in Fig. 8 a2) and 8 b2) for the H-charged case and the H-free case, respectively. A somewhat extended plastic zone is found to be produced just below the notch and seems to be left behind as a crack propagating farther ahead for the H-charged case. For the H-free case, a larger plastic zone can be found ahead of the crack, and it seems to move with the crack. Moreover, the crack margin is found to be surrounded by a region with less

dislocation density, indicating that dislocations are driven out by the high stress field at the crack tip, which is commonly observed as a dislocation free zone in some in situ TEM studies [47]. However, this is not the case in the H-charged sample, and a large dislocation density is found in the vicinity of the crack brims, implying that dislocations emitted from the crack tip are somehow blocked and cannot move away from the crack tip area. Further bending of the cantilever leads to an enhanced crack propagation in Stage 3 and a slight suppression in Stage 4. From the microstructure viewpoint, a very confined plastic zone along the cracking passageway is found at this stage, which is reasonable since the crack tip is now supposed to be sharper than the initial notch, and thus the highly concentrated stress field ahead of it will attract more H. The large amount of H present locally will further block the emission of dislocations, resulting in a stepped-up propagation with a more confined plastic zone. A slight suppression of the cracking rate in Stage 4 is observed when the crack steps into the compression zone near the bottom free surface, which shows a retarding effect for further propagation.
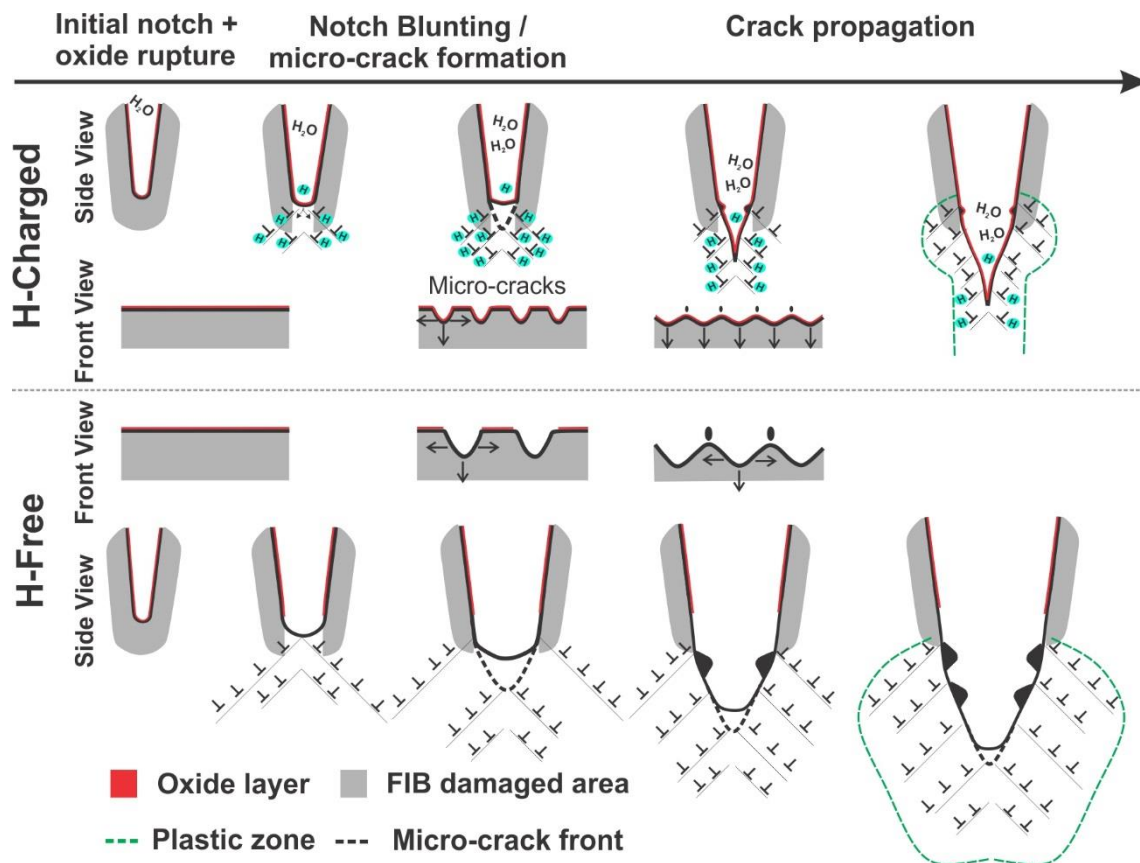

Fig. 9. Schematic representation of the crack tip deformation during propagation for H-charged and H-free cases.

Based on our experimental observation, we conclude a three-stage cracking process: the rupture of the oxide layer occurred on the elastic loading region (Stage I); the notch tip blunting and micro-crack nucleation (Stage II); and the stable crack propagation (Stage III).

In Stage I, the outermost oxide layer, which is considered to behave in a brittle manner, breaks up under the applied local strain near the notch tip. After the rupture of the oxide layer, the chemical reaction of H_2O with fresh FeAl metal occurs locally near the notch tip, where the H-uptake occurs simultaneously. The rupture of the oxide layer can start before the yielding of the material, like the H-uptake. The introduced H then facilitates the dislocation nucleation via reducing nucleation energy [48-50], so a reduced yielding force (~735 µN for H-free case and ~615 µN for H-charged case) or stress intensity for dislocation nucleation (2.41 MPa√m vs. 1.99 MPa√m) is observed.

In Stage II, dislocations are continuously generated from the notch tip and contribute to the notch tip blunting. The local stress field is then shielded with dislocations moving away from the notch tip. With further application of the external force, a gradual weakening of the shielding effect occurs due to increasing mutual interaction of dislocations via elastic stress field and/or reaction of dislocations from different slip planes to create dislocation locks. All of them will allow repulsive stress to hinder further dislocation movement. Thus, the stress intensity starts to grow locally, and some isolated micro-cracks will then be initiated along the notch front where K reaches the critical value for cracking. When nucleated, the micro-cracks will start to propagate both in the transverse direction by necking down the enclaves and in the vertical direction to travel farther ahead, leaving arrows of pyramid-like enclaves along the fracture surface (see Fig. 4 a2). The whole procedure will be accelerated when a high amount of H is present ahead of the notch tip. In addition to the two dislocation-blocking mechanisms mentioned above, the dislocation motion is further hindered by the presence of H, so both the micro-crack nucleation and micro-crack propagation processes are accelerated. The enclaves between the micro-cracks are observed to be much smaller and only appear very near to the notch end, as shown in Fig. 4 b2). The enclaves appear to resemble steps between each of the micro-cracks.

In Stage III, an accelerated crack propagation rate with a reduced bending force were found at this stage for both H-free and H-charged cases. The enhanced cracking rate is associated with the much sharper crack tip after stage II compared to the initial FIB induced notch and/or the propagation of the crack out of the FIB-damaged area (with Ga+ implantation). In this stage, the crack propagation is free of the notch radius and the Ga+ implantation influence and shows as much as possible the pure metal cracking behaviour. The fracture toughness values obtained with the J-integral from this stage by excluding the stage II (see Fig. 4) are notch geometry-independent and can be counted as pure material properties (15.5 MPa√m for the H-charged case and 23.6 MPa√m for the H-free case).

In bcc structure alloys, plastic deformation is carried mainly by the ½ <111> screw dislocations via the kink-pair nucleation and expansion. The enhanced kink-pair nucleation when exposed to H atmosphere has been reported via in situ electrochemical nanoindentation tests [48] and has been predicted by the thermodynamic defactant mechanism [51, 52]. The double-kink activation energy was found to decrease by the transition of H from a weaker binding site to a stronger one via the nudged elastic band method [25]. However, the H-reduced dislocation

mobility is quite the opposite to the HELP mechanism, which proposed an enhanced dislocation mobility result from a reduced degree of dislocation interaction with other elastic singularities due to the H shielding effect. This mechanism found popularity with the vast number of FCC alloys with very high H solubility, while for bcc alloys, the required H amount was estimated to be too high to be achievable in experiments [24]. Among the massive research into HE in bcc alloys, a few of them tried to correlate the phenomenon with dislocation mobility. Wen et al. [25] proposed that the sideward motion of the kink-pair is impeded by H through the nudged elastic band method. Song and Curtin [27] reported an increased critical KI for dislocation emission from crack tip with increasing H content, which indicates that the dislocation motion is blocked by the H. Recently, an in situ nano-pillar compression test was conducted in ETEM showing that mobile dislocations can lose mobility with activating stress more than double in Al when exposed to H gas. Together with atomistic simulation, the dislocation locking effect was associated with the superabundant hydrogenated vacancies [29]. This may also be the case in FeAl because of the large amount of structural vacancies present in the materials. The effect of vacancy content on the HE effect needs further analysis.

5. Conclusions

The hydrogen-assisted cracking phenomenon in FeAl intermetallic alloys was investigated by in situ fracture experiments using notched micrometre-sized specimens under in situ hydrogen charging and in situ imaging within ESEM.

1. A stable crack growth was obtained in all tested specimens under the current experimental settings. The whole cracking process was sped up when H is present. Three stages of crack growth were found: i) Elastic regime; ii) Notch blunting and micro-crack formation; and iii) Stable crack propagation. An additional 4th regime: crack suppression by the bottom surface, was found only in H-charged specimens due to the high crack growth velocity.

2. The hydrogen embrittlement phenomenon occurred by the strong hydrogen-dislocation interactions. The stress intensity for dislocation nucleation was found to be reduced by the presence of hydrogen in the 1st elastic regime (2.41 MPaVm in the H-free case and 1.99 MPaVm in the H-charged case). The micro-cracks in the 2nd regime, which are formed due to the suppression of dislocation mobility, were found to be easier in the H-charged specimens, indicating dislocation emission from the crack tip was inhibited under H exposure. Moreover, a very confined plastic zone near the crack brims observed from both t-EBSD and TEM BF analysis further verifies the restricted dislocation movement in the presence of highly concentrated hydrogen.

3. The combination of hydrogen-enhanced dislocation nucleation and hydrogen-reduced dislocation mobility results in an accelerated crack growth process and a reduced fracture toughness (23.6 MPaVm in the H-free case and 15.5 MPaVm in the H-charged case).

6. Acknowledgements

7. Reference:

[1]   D. Di Stefano, M. Mrovec, C. Elsässer. First-principles investigation of quantum mechanical effects on the diffusion of hydrogen in iron and nickel, Physical Review B 92 (2015).

[2]   P.G. Marsh, W.W. Gerberich. A microscopically-shielded Griffith criterion for cleavage in grain oriented silicon steel, Acta Metallurgica et Materialia 42 (1994) 613-619.

[3]   Z. Tarzimoghadam, M. Rohwerder, S.V. Merzlikin, A. Bashir, L. Yedra, S. Eswara, D. Ponge, D. Raabe. Multi-scale and spatially resolved hydrogen mapping in a Ni–Nb model alloy reveals the role of the δ phase in hydrogen embrittlement of alloy 718, Acta Materialia 109 (2016) 69-81.

[4]   A.R. Troiano, R. Gibala, R. Hehemann. Hydrogen embrittlement and stress corrosion cracking: a Troiano Festschrift, ASM International, 1984.

[5]   H. Vehoff, P. Neumann. Crack propagation and cleavage initiation in Fe-2.6%-Si single crystals under controlled plastic crack tip opening rate in various gaseous environments, Acta Metallurgica 28 (1980) 265-272.

[6]   H. Vehoff, W. Rothe. Gaseous hydrogen embrittlement in FeSi- and Ni-single crystals, Acta Matallurgica 31 (1983) 13.

[7]   H. Vehoff, W. Rothe. Gaseous hydrogen embrittlement in FeSi- and Ni-single crystals, Acta Metallurgica 31 (1983) 1781-1793.

[8]   W.W. Gerberich, R.A. Oriani, M.J. Lji, X. Chen, T. Foecke. The necessity of both plasticity and brittleness in the fracture thresholds of iron, Philosophical Magazine A 63 (1991) 363-376.

[9]   Y.A. Du, L. Ismer, J. Rogal, T. Hickel, J. Neugebauer, R. Drautz. First-principles study on the interaction of H interstitials with grain boundaries inα- andγ-Fe, Physical Review B 84 (2011).

[10]   Z. Tarzimoghadam, D. Ponge, J. Klöwer, D. Raabe. Hydrogen-assisted failure in Ni-based superalloy 718 studied under in situ hydrogen charging: The role of localized deformation in crack propagation, Acta Materialia 128 (2017) 365-374.

[11]   A. Laureys, T. Depover, R. Petrov, K. Verbeken. Influence of sample geometry and microstructure on the hydrogen induced cracking characteristics under uniaxial load, Materials Science and Engineering: A 690 (2017) 88-95.

[12]   A.M. Tahir, R. Janisch, A. Hartmaier. Hydrogen embrittlement of a carbon segregated Σ5(310)[001] symmetrical tilt grain boundary in α-Fe symmetrical tilt grain boundary in α-Fe, Materials Science and Engineering: A 612 (2014) 462-467.

[13]   S. Lynch. Hydrogen embrittlement phenomena and mechanisms, Corrosion Reviews 30 (2012).

[14]   S.P. Lynch. Environmentally assisted cracking: Overview of evidence for an adsorption-induced localised-slip process, Acta Metallurgica 36 (1988) 2639-2661.

[15]   M. Dadfarnia, M.L. Martin, A. Nagao, P. Sofronis, I.M. Robertson. Modeling hydrogen transport by dislocations, Journal of the Mechanics and Physics of Solids 78 (2015) 511-525.

[16]   S.D. House, J.J. Vajo, C. Ren, A.A. Rockett, I.M. Robertson. Effect of ball-milling duration and dehydrogenation on the morphology, microstructure and catalyst dispersion in Ni-catalyzed MgH2 hydrogen storage materials, Acta Materialia 86 (2015) 55-68.

[17]   M.L. Martin, J.A. Fenske, G.S. Liu, P. Sofronis, I.M. Robertson. On the formation and nature of quasi-cleavage fracture surfaces in hydrogen embrittled steels, Acta Materialia 59 (2011) 1601-1606.

[18]   M.L. Martin, I.M. Robertson, P. Sofronis. Interpreting hydrogen-induced fracture surfaces in terms of deformation processes: A new approach, Acta Materialia 59 (2011) 3680-3687.

[19]   M.L. Martin, P. Sofronis, I.M. Robertson, T. Awane, Y. Murakami. A microstructural based understanding of hydrogen-enhanced fatigue of stainless steels, International Journal of Fatigue 57 (2013) 28-36.

[20]   A. Nagao, M.L. Martin, M. Dadfarnia, P. Sofronis, I.M. Robertson. The effect of nanosized (Ti,Mo)C precipitates on hydrogen embrittlement of tempered lath martensitic steel, Acta Materialia 74 (2014) 244-254.

[21]   I.M. Robertson, P. Sofronis, A. Nagao, M.L. Martin, S. Wang, D.W. Gross, K.E. Nygren. Hydrogen Embrittlement Understood, Metallurgical and Materials Transactions B 46 (2015) 1085-1103.

[22]   S. Wang, M.L. Martin, P. Sofronis, S. Ohnuki, N. Hashimoto, I.M. Robertson. Hydrogen-induced intergranular failure of iron, Acta Materialia 69 (2014) 275-282.

[23]   H.K. Birnbaum, P. Sofronis. Hydrogen-enhanced localized plasticity—a mechanism for hydrogen-related fracture, Materials Science and Engineering: A 176 (1994) 191-202.

[24]   Y. Jagodzinski, H. Hänninen, O. Tarasenko, S. Smuk. Interaction of hydrogen with dislocation pile-ups and hydrogen induced softening of pure iron, Scripta materialia 43 (2000) 245-251.

[25]   M. Wen, S. Fukuyama, K. Yokogawa. Atomistic simulations of effect of hydrogen on kink-pair energetics of screw dislocations in bcc iron, Acta materialia 51 (2003) 1767-1773.

[26]   S. Taketomi, R. Matsumoto, N. Miyazaki. Molecular Statics Study of the Effect of Hydrogen on Edge Dislocation Motion in Alpha-Fe. in: Somerday BP, Sofronis P, (Eds.). International Hydrogen Conference (IHC 2012). ASME, New York, NY, 2014.

[27]   J. Song, W.A. Curtin. Atomic mechanism and prediction of hydrogen embrittlement in iron, Nature materials 12 (2013) 145-151.

[28]   J. Song, W.A. Curtin. Mechanisms of hydrogen-enhanced localized plasticity: An atomistic study using α-Fe as a model system, Acta Materialia 68 (2014) 61-69.

[29]   D. Xie, S. Li, M. Li, Z. Wang, P. Gumbsch, J. Sun, E. Ma, J. Li, Z. Shan. Hydrogenated vacancies lock dislocations in aluminium, Nature communications 7 (2016) 13341.

[30]   M. Hatano, M. Fujinami, K. Arai, H. Fujii, M. Nagumo. Hydrogen embrittlement of austenitic stainless steels revealed by deformation microstructures and strain-induced creation of vacancies, Acta Materialia 67 (2014) 342-353.

[31]   I.M. Robertson. The effect of hydrogen on dislocation dynamics, Engineering Fracture Mechanics 68 (2001) 671-692.

[32]   A. Barnoush, N. Kheradmand, T. Hajilou. Correlation between the hydrogen chemical potential and pop-in load during in situ electrochemical nanoindentation, Scripta Materialia 108 (2015) 76-79.

[33]   Y. Deng, T. Hajilou, D. Wan, N. Kheradmand, A. Barnoush. In-situ micro-cantilever bending test in environmental scanning electron microscope: Real time observation of hydrogen enhanced cracking, Scripta Materialia 127 (2017) 19-23.

[34]   T. Hajilou, Y. Deng, B.R. Rogne, N. Kheradmand, A. Barnoush. In situ electrochemical microcantilever bending test: A new insight into hydrogen enhanced cracking, Scripta Materialia 132 (2017) 17-21.

[35]   Y. Deng, T. Hajilou, A. Barnoush. Hydrogen-enhanced cracking revealed by in situ micro-cantilever bending test inside environmental scanning electron microscope, Philosophical Transactions of the Royal Society A: Mathematical, Physical and Engineering Sciences 375 (2017).

[36]   P. Specht, M. Brede, P. Neumann. Fracture Toughness, Fracture Planes and BDT in Stoichiometric Feal and Nial Single Crystals, MRS Proceedings 364 (1994).

[37]   R.R. Keller, R.H. Geiss. Transmission EBSD from 10 nm domains in a scanning electron microscope, Journal of Microscopy 245 (2012) 245-251.

[38]   E 399-490: Standard Test Method for Plane-Strain Fracture Toughness of Metallic Materials. ASTM International, West Conshohocken, PA, 1997.

[39]   F. Iqbal, J. Ast, M. Göken, K. Durst. In situ micro-cantilever tests to study fracture properties of NiAl single crystals, Acta Materialia 60 (2012) 1193-1200.

[40]   D. Guedes, A. Oudriss, S. Frappart, G. Courlit, S. Cohendoz, P. Girault, J. Creus, J. Bouhattate, A. Metsue, F. Thebault, L. Delattre, D. Koschel, X. Feaugas. The influence of hydrostatic stress states on the hydrogen solubility in martensitic steels, Scripta Materialia 84-85 (2014) 23-26.

[41]   M. Göken, F. Thome, H. Vehoff. Study of crack tip deformation in FeAl and NiAl crystals with optical interference microscopy and atomic force microscopy, Philosophical Magazine A 82 (2002) 3241-3250.

[42]   E1820: Standard Test Method for Measurement of Fracture Toughness. ASTM International, West Conshohocken, PA, 1997.

[43]   M.H. Yoo, C.L. Fu. Cleavage fracture of ordered intermetallic alloys, Materials Science and Engineering: A 153 (1992) 470-478.

[44]   P. Specht, P. Neumann. Fracture planes and toughness of stoichiometric FeAl single crystals, Intermetallics 3 (1995) 365-368.

[45]   E. Demir, D. Raabe, F. Roters. The mechanical size effect as a mean-field breakdown phenomenon: Example of microscale single crystal beam bending, Acta Materialia 58 (2010) 1876-1886.

[46]   P. Neumann. The geometry of slip processes at a propagating fatigue crack—II, Acta Metallurgica 22 (1974) 1167-1178.

[47]   S.M. Ohr. An electron microscope study of crack tip deformation and its impact on the dislocation theory of fracture, Materials Science and Engineering 72 (1985) 1-35.

[48]   A. Barnoush, J. Dake, N. Kheradmand, H. Vehoff. Examination of hydrogen embrittlement in FeAl by means of in situ electrochemical micropillar compression and nanoindentation techniques, Intermetallics 18 (2010) 1385-1389.

[49]   A. Barnoush, H. Vehoff. Recent developments in the study of hydrogen embrittlement: Hydrogen effect on dislocation nucleation, Acta Materialia 58 (2010) 5274-5285.

[50]   G.P.M. Leyson, B. Grabowski, J. Neugebauer. Multiscale modeling of hydrogen enhanced homogeneous dislocation nucleation, Acta Materialia 107 (2016) 144-151.

[51]   R. Kirchheim. Revisiting hydrogen embrittlement models and hydrogen-induced homogeneous nucleation of dislocations, Scripta Materialia 62 (2010) 67-70.

[52]   R. Kirchheim, B. Somerday, P. Sofronis. Chemomechanical effects on the separation of interfaces occurring during fracture with emphasis on the hydrogen-iron and hydrogen-nickel system, Acta Materialia 99 (2015) 87-98.

8.   Supplementary Materials:

8.1.   The loading procedure for cantilever shown in Fig. 3a
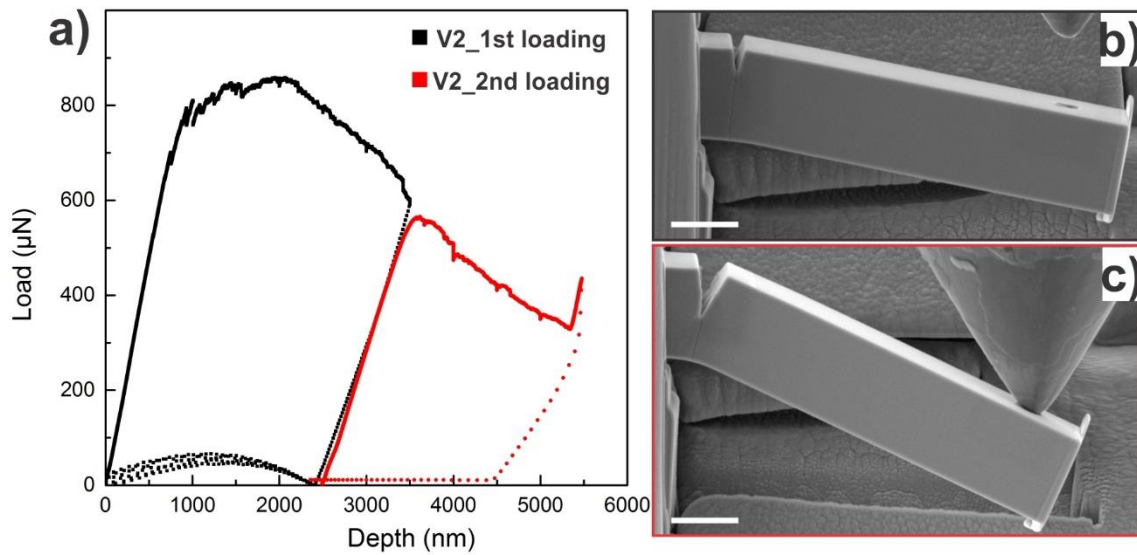
Fig. 10. The loading processes of cantilever V2 a): the side view after 1st loading b) and after 2nd loading c). Beyond the two normal loading procedures, an additional quick hit was applied to open the crack mouth far enough to observe the fracture surface. The side view and fracture surface of V2 after the quick hit are shown in Fig. 3a1 and a2. All the scale bars are 2 μm.

8.2.   *t-EBSD vs normal EBSD*

Fig. 11